# Characterization of optical nonlinearities in nanoporous silicon waveguides via pump-probe heterodyning technique

**Ryan J. Suess,* Mohammad M. Jadidi, Kyowon Kim, and Thomas E. Murphy**

*Institute for Research in Electronics and Applied Physics*
*University of Maryland, College Park, MD 20742, USA*

*rjsuess@umd.edu

**Abstract:** The nonlinear response of nanoporous silicon optical waveguides is investigated using a novel pump-probe method. In this approach we use a two-frequency heterodyne technique to measure the pump-induced transient change in phase and intensity in a single measurement. We measure a 100 picosecond material response time and report behavior matching a physical model dominated by free-carrier effects significantly stronger than those observed in traditional silicon-based waveguides.



**OCIS codes:** (160.4330) Nonlinear optical materials; (160.4236) Nanomaterials; (230.7370) Waveguides; (120.0120) Instrumentation, measurement, and metrology.

## References and links

1. M. Hochberg and T. Baehr-Jones, "Towards fabless silicon photonics," Nat. Photon. **4**, 492–494 (2010).
2. B. Jalali and S. Fathpour, "Silicon photonics," J. Lightwave Technol. **24**, 4600–4615 (2006).
3. G. T. Reed and A. P. Knights, *Silicon Photonics* (Wiley, 2008).
4. D. Dimitropoulos, R. Jhaveri, R. Claps, J. Woo, and B. Jalali, "Lifetime of photogenerated carriers in silicon-on-insulator rib waveguides," Appl. Phys. Lett. **86**, 071115 (2005).
5. A. Agarwal, L. Liao, J. Foresi, M. R. Black, X. Duan, and L. Kimerling, "Low-loss polycrystalline silicon waveguides for silicon photonics," J. Appl. Phys. **80**, 6120–6123 (1996).
6. A. Harke, M. Krause, and J. Mueller, "Low-loss singlemode amorphous silicon waveguides," Electron. Lett. **41**, 1377–1379 (2005).
7. A. Cullis, L. T. Canham, and P. Calcott, "The structural and luminescence properties of porous silicon," J. Appl. Phys. **82**, 909–965 (1997).
8. G. Vincent, "Optical properties of porous silicon superlattices," Appl. Phys. Lett. **64**, 2367–2369 (1994).
9. P. Apiratikul, A. M. Rossi, and T. E. Murphy, "Nonlinearities in porous silicon opticalwaveguides at 1550 nm," Opt. Express **17**, 3396–3406 (2009).
10. R. J. Suess and T. E. Murphy, "Third-order optical nonlinearity in bulk nanoporous silicon at telecom wavelengths," in "CLEO: Applications and Technology" (Optical Society of America, 2012).
11. F. Z. Henari, K. Morgenstern, W. J. Blau, V. A. Karavanskii, and V. S. Dneprovskii, "Third-order optical nonlinearity and all-optical switching in porous silicon," Appl. Phys. Lett. **67**, 323–325 (1995).
12. T. Matsumoto, M. Daimon, H. Mimura, Y. Kanemitsu, and N. Koshida, "Optically induced absorption in porous silicon and its application to logic gates," J. Electrochem. Soc. **142**, 3528–3533 (1995).
13. H. Föll, M. Christophersen, J. Carstensen, and G. Hasse, "Formation and application of porous silicon," Mat. Sci. Eng. R **39**, 93–141 (2002).
14. W. Theiß, "Optical properties of porous silicon," Surf. Sci. Rep. **29**, 91–192 (1997).
15. K. Kim and T. E. Murphy, "Porous silicon integrated mach-zehnder interferometer waveguide for biological and chemical sensing," Opt. Express **21**, 19488–19497 (2013).
16. R. Hui and M. O'Sullivan, *Fiber Optic Measurement Techniques* (Academic, 2009).

#212659 - $15.00 USD Received 22 May 2014; revised 25 Jun 2014; accepted 26 Jun 2014; published 10 Jul 2014

17. P. Apiratikul, "Semiconductor waveguides for nonlinear optical signal processing," Ph.D. thesis, University of Maryland, College Park (2009).
18. K. L. Hall, G. Lenz, E. P. Ippen, and G. Raybon, "Heterodyne pump–probe technique for time-domain studies of optical nonlinearities in waveguides," Opt. Lett. **17**, 874–876 (1992).
19. Y. Shoji, T. Ogasawara, T. Kamei, Y. Sakakibara, S. Suda, K. Kintaka, H. Kawashima, M. Okano, T. Hasama, H. Ishikawa, and M. Mori, "Ultrafast nonlinear effects in hydrogenated amorphous silicon wire waveguide," Opt. Express **18**, 5668–5673 (2010).
20. P. A. Elzinga, R. J. Kneisler, F. E. Lytle, Y. Jiang, G. B. King, and N. M. Laurendeau, "Pump/probe method for fast analysis of visible spectral signatures utilizing asynchronous optical sampling," Appl. Opt. **26**, 4303–4309 (1987).
21. T. Matsumoto, T. Futagi, H. Mimura, and Y. Kanemitsu, "Ultrafast decay dynamics of luminescence in porous silicon," Phys. Rev. B **47**, 13876–13879 (1993).
22. R. Tsu, H. Shen, and M. Dutta, "Correlation of raman and photoluminescence spectra of porous silicon," Appl. Phys. Lett. **60**, 112–114 (1992).
23. R. Soref and B. Bennett, "Electrooptical effects in silicon," IEEE J. Quantum Electron. **23**, 123–129 (1987).
24. A. Cutolo, M. Iodice, P. Spirito, and L. Zeni, "Silicon electro-optic modulator based on a three terminal device integrated in a low-loss single-mode soi waveguide," J. Lightwave Technol. **15**, 505–518 (1997).
25. X. Gai, Y. Yu, B. Kuyken, P. Ma, S. J. Madden, J. Campenhout, P. Verheyen, G. Roelkens, R. Baets, and B. Luther-Davies, "Nonlinear absorption and refraction in crystalline silicon in the mid-infrared," Laser Photon. Rev. **7**, 1054–1064 (2013).
26. D. Lockwood, "Optical properties of porous silicon," Solid State Commun. **92**, 101–112 (1994).
27. O. E. DeLange, "Optical heterodyne detection," IEEE Spectrum **5**, 77–85 (1968).
28. R. H. Kingston, *Optical Sources, Detectors, and Systems: Fundamentals and Applications* (Academic, 1995).
29. W. Hou and X. Zhao, "Drift of nonlinearity in the heterodyne interferometer," Precis. Eng. **16**, 25–35 (1994).
30. C.-K. Sun, B. Golubovic, J. Fujimoto, H. Choi, and C. Wang, "Heterodyne nondegenerate pump–probe measurement technique for guided-wave devices," Opt. Lett. **20**, 210–212 (1995).
31. A. R. Motamedi, A. H. Nejadmalayeri, A. Khilo, F. X. Kärtner, and E. P. Ippen, "Ultrafast nonlinear optical studies of silicon nanowaveguides," Opt. Express **20**, 4085–4101 (2012).

## 1. Introduction

The interest in silicon photonics has been motivated by the possibility of leveraging mature semiconductor processing technology to manufacture low-cost, integrated electronic and photonic components on a single chip [1–3]. Though silicon is transparent in the near-infrared, its indirect band gap and long carrier lifetime [4] have generated interest in silicon alternatives with more desirable optical properties [5–7]. One such material is nanoporous silicon (pSi), which is composed of a remnant irregular silicon framework permeated by nanometer scale, air-filled pores and formed through an electrochemical etching process. Porous silicon has the appealing property that its effective refractive index can be well controlled during the fabrication process [8] to form waveguides and other layered dielectric structures.

Despite the potential of pSi as a material for optical devices, there have been relatively few studies investigating the behavior of pSi at the technologically important wavelength of 1550 nm. Earlier studies at this wavelength [9, 10] have indicated exceptionally large and fast carrier-based optical nonlinearities in this material. In this study, we carry out definitive measurements on pSi waveguides using a novel pump-probe technique that unambiguously characterizes both the magnitude and phase of the nonlinear response in a single measurement. A simple model establishes that the enhancement in the nonlinearity is due to short-lived free-carriers in the nanoporous silicon, indicating a potential pathway for new devices based on these effects. These results encourage further studies of pSi waveguides as a viable platform for application areas such as all-optical switching [11] and optical logic gates [12].

The work presented here is organized in the following manner: The "Fabrication and experimental setup" section provides details regarding the pSi waveguide fabrication and characterization methods. The essential features of the experimental setup used to characterize the nonlinear optical properties of the pSi waveguides are also discussed. The section "Experimental results and discussion" presents the transient relative intensity and phase response for the pSi

#212659 - $15.00 USD Received 22 May 2014; revised 25 Jun 2014; accepted 26 Jun 2014; published 10 Jul 2014

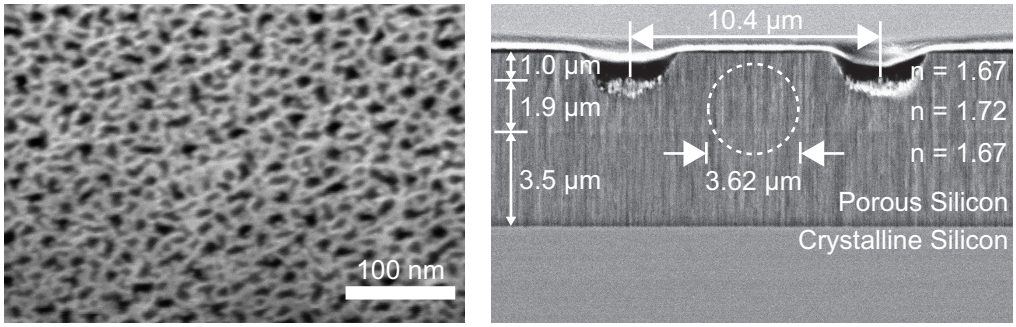


Fig. 1. Scanning electron micrographs showing nanoporous silicon structure (a) and the waveguide end facet of the type characterized in this study (b). The dashed circle shows the approximate mode dimension as estimated by a diffraction technique described in the text. The polymer cover layer (appearing as the topmost material in (b)) was not present during device characterization.

waveguide. Data showing the power dependence of the optical nonlinearity are also presented. A simple model incorporating carrier-based effects is developed and the instantaneous and free-carrier nonlinear coefficients are estimated and shown to be dramatically different from those observed in silicon-on-insulator (SOI) waveguides. An appendix is also provided and gives a detailed discussion of the two-frequency heterodyne method.

## 2. Fabrication and experimental setup

Porous silicon is formed by electrochemically etching a conductive silicon substrate. The columnar pores, which are oriented perpendicular to the silicon wafer surface plane and along the same direction as the applied current, form naturally with the proper choice of wafer doping, crystallographic direction, etchant solution chemistry, and applied current [13, 14]. The amount of silicon removed is in direct proportion to the applied current, thereby enabling the formation of 1-dimension profiles of varying silicon volume fraction by controlling the current during the etching process. A representative nanoporous silicon structure is shown in the top-down scanning electron micrograph shown in Fig. 1(a). The waveguides tested in this study utilized a current-controlled electrochemical etch that produced a buried optical slab waveguide with a 1.9 µm core with an effective refractive index of $n = 1.72$ surrounded on each side by $n = 1.67$ cladding layers. To confine the optical mode in the second transverse direction, a computer controlled laser ablation writing system was used to fabricate two parallel trenches on the surface of the porous silicon wafer having a length and spacing that define respectively the length and width of the optical waveguide. The waveguide refractive index profile and width are designed to support single mode operation at 1560 nm. An optical micrograph showing the device fabricated as described above is shown in Fig. 1(b). Full details of the pSi optical waveguide fabrication and characterization process are given in [9, 15].

The linear propagation loss of the waveguide was estimated by performing cutback measurements [16] for devices of different lengths. This approach produced a loss estimate of 13.5 dB/cm; indicating 7.7 dB of total loss attributed to linear absorption for the 0.57 cm long waveguide. There are several factors that contribute to this linear loss, including Rayleigh scattering from the nanoporous structure, edge roughness from the laser-patterned waveguide boundaries, residual free-carrier absorption, and transverse evanescent leakage. Inverse transmission measurements [17] were used to estimate the free-space input coupling loss and the

#212659 - $15.00 USD Received 22 May 2014; revised 25 Jun 2014; accepted 26 Jun 2014; published 10 Jul 2014

two-photon absorption coefficient, $\beta_{2PA}$, and found to be 5.25 dB and 1.15 cm/GW respectively. The optical mode size was estimated by a observing the far-field diffraction of the the light exiting from the back facet of the waveguide. The measured beam divergence is nearly symmetric and Gaussian, from which a mode size of 10.27 $\mu m^2$ is inferred. The inferred mode profile is overlaid on the micrograph in Fig. 1(b).

To characterize the nonlinear optical properties of the waveguides, a two-frequency pump-probe heterodyne technique was used. The experimental setup used in this study differs slightly from more conventional pump-probe heterodyne techniques [18, 19] and is diagrammed in Fig. 2. As with traditional pump-probe heterodyning, the two-frequency approach uses a reference pulse, chopped pump pulse, and probe pulse that are sequentially launched into the waveguide, with a variable delay $\tau$ between the pump and probe pulse. After traversing the waveguide, the reference and probe pulses are temporally overlapped at the detector using a Michelson interferometer to produce a heterodyne signal (see Fig. 2). The amplitude and phase of the probe pulse is modified due to the presence of the pump in the sample, thus altering the magnitude and phase of the heterodyne signal measured by the lock-in amplifier. Measuring the amplitude and phase change as a function of pump delay time ($\tau$) gives the transient absorption and phase response, respectively.

The chopping of the pump beam introduces additional tones above and below the heterodyne frequency. By using a lock-in amplifier that is capable of measurement at two different reference frequencies (the heterodyne frequency and the first upper sideband due to the chopping), it is possible to simultaneously determine both the magnitude and phase of the probe pulse. The dual-frequency measurement described here determines the only the relative changes in intensity and phase that are caused by the chopping of the pump signal, and is hence insensitive to slow phase fluctuations and drift that otherwise plague heterodyne measurements.

The pump pulse is produced by a 100 MHz mode-locked fiber-laser (Menlo Systems), and the probe and reference pulses are obtained from a second, similar mode-locked laser. The two lasers have intra-cavity piezoelectric actuators that allow for fine adjustment of their repetition rates. Using external synchronization circuitry, the two lasers are locked together with a small difference frequency $\delta f = 0.1$ mHz, thereby producing a slow, linear sweep of the time delay $\tau$ between the pump and probe. This allows for large delays (nanoseconds for the system used in this study) without the use of mechanical delay lines [20]. Both lasers are co-polarized and have a center wavelength of 1.56 μm and a pulsewidth of 100 fs (FWHM).

The time delay $T$ between the probe and reference is set to 830 ps using a fixed external delay line. This delay limits the maximum pump-probe delay that can be unambiguously measured in the experiment. The reference and probe pulses are derived from the same laser and are frequency blue-shifted by frequencies of $f_D = 35$ MHz and $f_D + f_H = 35.0625$ MHz respectively using a pair of acousto-optic frequency shifters (AOFS). The difference frequency between the two AOFSs defines the heterodyne frequency, which was set to $f_H = 62.5$ kHz for this study. The AOFS causes the probe and references pulses to broaden to approximately 700 fs, as determined by autocorrelation measurements at the output.

The pump beam, which is chopped at frequency $f_c = 1$ kHz, is combined with the probe and reference beams and passed through a polarizing beam cube, resulting in an horizontally polarized beam impinging on the waveguide end facet. The ratio of the pump power to the combined probe and reference beam power (the probe and reference beams are equipotent) can be controlled with half-wave plates (HWP) prior to beam combination and ranged between 35 and 70 for the measurements reported here.

The light is next free-space coupled into the TE eigenmode of the waveguide using an 0.65 NA 60× aspheric lens. The electric field of the TE mode is perpendicular to the principal direction of the columnar pores, resulting in a lower linear propagation loss in comparison to

#212659 - $15.00 USD Received 22 May 2014; revised 25 Jun 2014; accepted 26 Jun 2014; published 10 Jul 2014

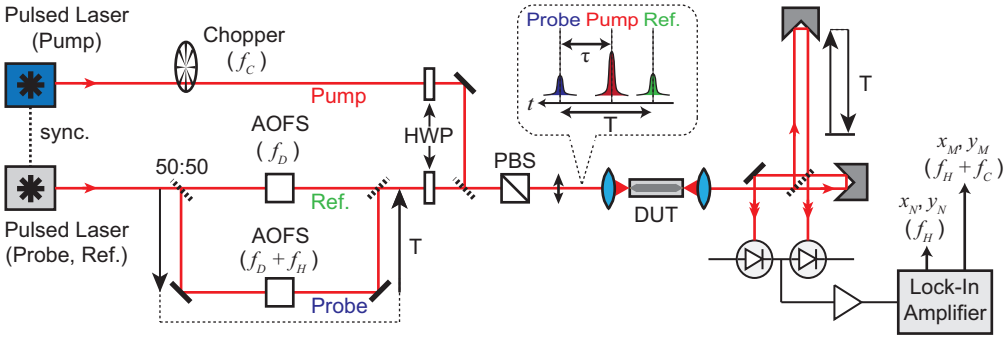


Fig. 2. Diagram of pump-probe experiment used in this study. The inset shows the relative timing of pulses incident on the device under test (DUT). A dual-phase lock-in amplifier measures the in-phase and quadrature components ($x$ and $y$ respectively) at two different frequencies $f_H$ and $f_H + f_C$. AOFS: acousto-optic frequency shifter; HWP: half waveplate; PBS: polarizing beam splitter.

the TM eigenmode. At the back facet of the waveguide, the emerging light is re-collimated and directed into a Michelson interferometer with a temporal path difference of $T$, chosen to temporally overlap the reference and probe pulses. Both outputs of the interferometer are differentially detected in a balanced photoreceiver to reduce the large common mode pump signal. A dual-phase digital lock-in amplifier (Signal Recovery 7270) is used to simultaneously detect both quadratures at both the heterodyne frequency, $f_H$, and at the first upper sideband of the heterodyne, $f_H + f_C$, which is generated by a nonlinear interaction with the pump pulse in the waveguide. The AOFSs, optical chopper, and lock-in reference signal are all derived from a common 4-channel synthesizer (Novatech 409B), thereby ensuring a common phase relation between the heterodyne and chopping frequency. The Appendix explains how these two-frequency measurements can be used to calculate the transient change in relative intensity and phase in a manner that is robust to noise, including a complete derivation of the relevant equations.

## 3. Experimental results and discussion

The experimental method described in the previous section was used to measure the time domain characteristics of the nonlinear optical properties of the pSi waveguides. Figure 3(a) shows the measured transient intensity change of the probe, $(\Delta I/I)$, as a function of the pump-probe delay, $\tau$. The inset shows an enlarged view near zero delay for three different coupled pump intensities. The absorption of the probe pulse is caused by a combination of instantaneous two-photon absorption of the pump and probe signal and subsequent free-carrier absorption caused by the associated electrons and holes.

The transient data reveals that multiple recombination time scales exist for the pSi waveguides measured in this study, as has been previously observed in photoluminescence studies in bulk pSi [21]. The intensity exhibits an initial exponential recovery with a $1/e$ recovery time of $\tau_c = 10$ ps, as depicted in the inset to Fig. 3(a), followed by a slower recovery. The 90% recovery time for free-carrier absorption in the pSi waveguides was found to be 100 ps. This result is several times faster than absorption-based measurements in conventional SOI waveguides of comparable geometry [4,9] which have lifetimes on the scale of $\tau_c = 1$ ns, and is orders of magnitude faster than the carrier lifetime in bulk silicon. The rapid recombination time is believed to originate in reduced mean free path lengths in the carrier diffusion process due to

#212659 - $15.00 USD Received 22 May 2014; revised 25 Jun 2014; accepted 26 Jun 2014; published 10 Jul 2014

the presence of local surface recombination sites in the nanoporous material [21].

Figure 4(a) plots the corresponding phase as a function of delay, which shows both an ultrafast decrease caused by instantaneous cross-phase modulation, followed by a slower positive phase shift caused by free-carrier dispersion. As with the intensity measurements, the free-carrier response exhibits a 90% recovery time of approximately 100 ps.

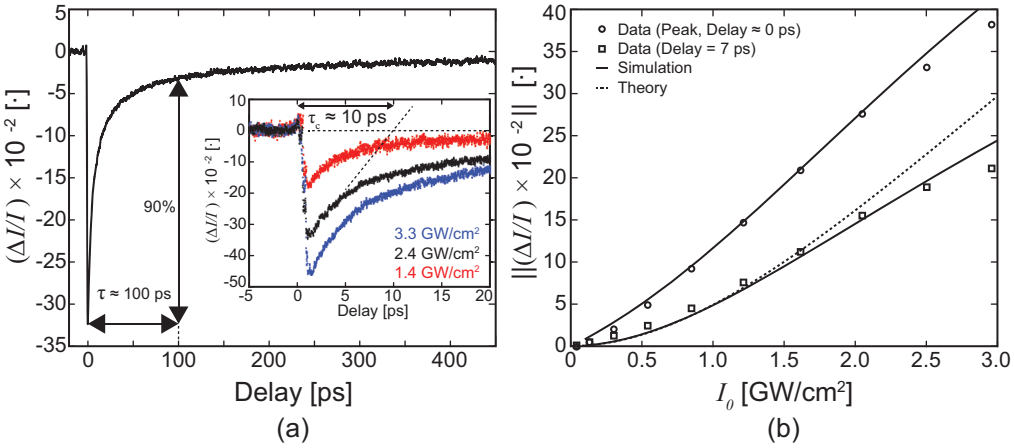


Fig. 3. (a) Transient normalized change in probe intensity for coupled pump intensity of 2.4 GW/cm$^2$. The inset shows a zoomed view of transient near zero delay for different coupled pump intensities (1.4, 2.4, 3.3 GW/cm$^2$ top to bottom). An effective time constant for the initial recovery is also indicated on the inset. (b) Relative change in probe intensity for delays $\tau = 0$ ps (top curve) and $\tau = 7$ ps (bottom curve) for varying coupled pump intensity. The theoretical curve (dotted line) is an approximate solution valid at low intensities.

In order to quantify the strength of the instantaneous and carrier-based nonlinearities, we measured the dependence of the transient magnitude and phase on the pump intensity. Figures 3(b) and 4(b) show the relative change in intensity and the change in phase as a function of the coupled pump peak intensity, for fixed values of pump-probe delay. In these plots we examine the intensity and phase dependence near zero delay, where we expect ultrafast effects such as two-photon absorption and the optical Kerr effect to dominate the response, and also the at 7 ps, where we anticipate effects predominantly from free-carriers generated by the strong pump.

The data was modeled by numerically solving the coupled equations of evolution for the reference, pump, and probe pulses in the presence of ultrafast optical nonlinearities and carrier-based effects. The equation governing pulse propagation is given by:

$$\frac{\partial}{\partial z}u(z,t) = \left[-\frac{\alpha}{2} + \left(i\frac{\omega}{c}n_2 - \frac{\beta_{2\mathrm{PA}}}{2}\right)\frac{|u(z,t)|^2}{A_{\mathrm{eff}}} - \left(i\frac{\omega}{c}\Delta n_{\mathrm{FCD}}(z,t) + \frac{1}{2}\Delta\alpha_{\mathrm{FCA}}(z,t)\right)\right]u(z,t) \tag{1}$$

where $u(z,t)$ represents the field envelopes including the pump, reference, and probe pulses, $\alpha$ is the linear absorption coefficient, $n_2$ is the Kerr coefficient, $\beta_{2\mathrm{PA}}$ corresponds to the two-photon absorption coefficient, and $A_{\mathrm{eff}}$ is the effective area of the optical mode. The coefficients

#212659 - $15.00 USD Received 22 May 2014; revised 25 Jun 2014; accepted 26 Jun 2014; published 10 Jul 2014

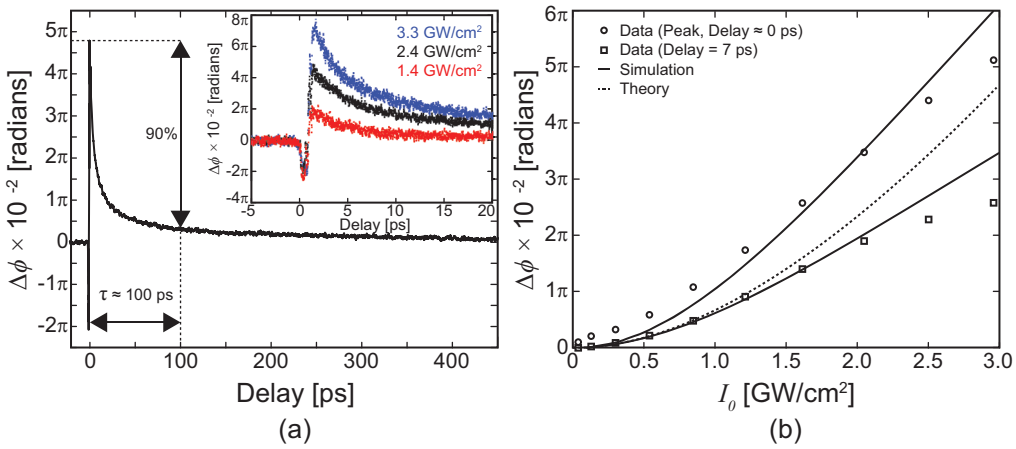


Fig. 4. (a) Change in phase for coupled pump intensity of 2.4 GW/cm$^2$. The inset shows a zoomed view of transient change in phase near zero delay for different intensities (1.4, 2.4, 3.3 GW/cm$^2$ bottom to top). (b) Change in phase for delays $\tau = 0$ ps (top curve) and $\tau = 7$ ps (bottom curve) for varying coupled pump intensity. The theoretical curve (dotted line) is an approximate solution valid at low intensities.

$\Delta\alpha_{\mathrm{FCA}}$ and $\Delta n_{\mathrm{FCD}}$ are related to the free-carrier population through the following relations:

$$\Delta\alpha_{\mathrm{FCA}}(z,t) = \sigma_{\mathrm{FCA}}\Delta N(z,t) \tag{2}$$

$$\Delta n_{\mathrm{FCD}}(z,t) = k_{\mathrm{FCD}}\Delta N(z,t) \tag{3}$$

where $\sigma_{\mathrm{FCA}}$ is the free-carrier absorption cross section and $k_{\mathrm{FCD}}$ is the free-carrier dispersion coefficient. The term $\Delta N(z,t)$ is the excess carrier density present in the waveguide caused by the strong pump pulse. The carrier density is related to the pump field in the waveguide by:

$$\frac{\partial}{\partial t}\Delta N(z,t) = \frac{\beta_{2\mathrm{PA}}}{2\hbar\omega}\left[\frac{|u(z,t)|^2}{A_{\mathrm{eff}}}\right]^2 - \frac{\Delta N(z,t)}{\tau_c} \tag{4}$$

with $\tau_c$ being the carrier recombination time, which was inferred from the transient measurements of Figs. 3 and 4. Second-order dispersion is excluded in Eq. (1) because the waveguides considered are not long enough to cause significant broadening of the 100 fs pulses used in the measurement. The Raman contribution to the nonlinear susceptibility was omitted in Eq. (1) because the pulses used in this experiment do not have sufficient bandwidth or spectral separation to efficiently couple through the vibrational modes of the crystal. Earlier measurements have shown that the Raman spectrum in porous silicon is only moderately broadened and shifted and otherwise retains many of the characteristics of the original silicon substrate [22].

The split-step Fourier method was implemented to solve the coupled equations for all pulses in the experiment and produce numerical $(\Delta I/I)$ and $\Delta\phi$ curves. The fitting was done simultaneously for all the data given in Figs. 3(b) and 4(b) and are shown as solid black lines. Fit parameters produced from the numerical solution give $\sigma_{\mathrm{FCA}} = 137\times10^{-17}$ cm$^2$ and $k_{\mathrm{FCD}} = 13.5\times10^{-21}$ cm$^3$. The fit value for the free-carrier absorption in pSi waveguides is two orders in magnitude larger than those for SOI waveguides while the free-carrier plasma dispersion is approximately 3 times larger. For bulk silicon, the free-carrier parameters have been reported in the literature as [23] $\sigma_{\mathrm{FCA,Si}} = 1.45\times10^{-17}$ cm$^2$ and $k_{\mathrm{FCD,Si}} = 3.5-7.5\times10^{-21}$ cm$^3$ [9, 24]. We note that these measurements are consistent with earlier reports that also show

#212659 - $15.00 USD Received 22 May 2014; revised 25 Jun 2014; accepted 26 Jun 2014; published 10 Jul 2014

a significant enhancement in the free-carrier parameters compared to crystalline silicon [9]. Unlike earlier measurements, which relied upon indirect estimates of the free-carrier dispersion and nonlinear refraction coefficients based only on spectral measurements, the present approach provides a direct measurement of the temporal phase response, which enables a less ambiguous determination of these parameters. Also notable in the data is the optical Kerr effect which is apparent immediately after zero delay in the inset of Fig. 4(a) and appears as a negative change in phase. Estimates for the Kerr coefficient produced by the full numerical solution gives $n_2 = 6.7 \times 10^{-14}$ cm$^2$/W; comparable to that of crystalline silicon [9].

Approximate solutions for the probe field, and hence approximate $(\Delta I/I)$ and $\Delta\phi$ curves, can be found for delay values larger than zero delay ($\tau \gg T_0$), once the strong pump pulse arriving at time zero is no longer present. Assuming weak probe and reference pulses, the probe pulse evolution dynamics are dominated primarily by the pump generated free-carrier population. Thus for times after the initial transient, the change in phase and relative intensity should be related to the carrier population. For carrier lifetimes $\tau_c \gg T_0$, the initial carrier population can be determined by integrating the pump intensity squared over the total duration of the pump pulse and will be a function of the initial coupled pump power and position. Furthermore, the net change in phase or relative intensity is given by the integral of the carrier population over the length of the waveguide. An approximate solution for the pump is assumed, which incorporates linear loss and two-photon absorption effects and assumes a $\mathrm{sech}^2(t/T_0)$ temporal dependence. The probe evolution is then given by the solution of Eq. (1) with only linear absorption and carrier-based effects included. The approximate probe field is given by:

$$u_{\mathrm{probe}}(t) = u_{0,\mathrm{probe}}(t-\tau)\exp\left(-\frac{\alpha}{2}L\right)\exp\left\{-\left(\frac{1}{2}\sigma_{\mathrm{FCA}} + i\frac{\omega}{c}k_{\mathrm{FCD}}\right)\right.$$
$$\left.\times\left[\frac{\beta_{\mathrm{2PA}}}{2\hbar\omega}\int_0^L\int_{-\infty}^{\tau} I^2_{\mathrm{pump}}(z,t';I_{0,\mathrm{pump}})dt'dz\right]e^{-t/\tau_c}\right\} \tag{5}$$

In the above expression $u_{0,\mathrm{probe}}$ is the temporal field envelope, $I_{\mathrm{Pump}}(z,t';I_{0,\mathrm{Pump}})$ is the pump intensity ansatz which has linear and two-photon absorption effects included, and $I_{0,\mathrm{Pump}}$ is the initial coupled pump input intensity. From the probe field solution, $(\Delta I/I)$ and $\Delta\phi$ can be calculated and are plotted as a dashed line in Figs. 3(b) and 4(b). The theoretical curves are an excellent match to the numerical solution and data taken at 7 ps delay for low intensities; supporting the claim that the observed effect is predominantly the result of free-carriers generated by the pump. For small coupled input intensities, the 7 ps delay data and theoretical curves are quadratic with power as expected. For larger values of intensity, the pump is depleted by two photon absorption and a sub-quadratic power dependence is observed. At higher intensities ($\geq$ 1.5 GW/cm$^2$) the theoretical and numerical solution diverge, with the theoretical curves over-predicting the nonlinear effects. This is expected as the theory does not incorporate the nonlinear absorption of the pump from self generated carriers, which further limits the amount of carriers generated at high intensities.

## 4. Conclusion

We reported the first measurements of the combined transient intensity and phase response for pSi optical waveguides. The transient response revealed carrier recombination lifetimes for both absorptive and refractive nonlinearities approximately 10 times faster than those observed in comparatively sized SOI waveguides. This enhancement in lifetime is the likely result of increased carrier accessibility to recombination sites on the surface of the nanoscale pores [14, 21]. Additionally, the magnitude of both the intensity and phase effects in pSi were observed to be exceedingly large relative to crystalline silicon-based waveguides. For

#212659 - $15.00 USD Received 22 May 2014; revised 25 Jun 2014; accepted 26 Jun 2014; published 10 Jul 2014

our waveguides, we measure a free-carrier cross section of $\sigma_{FCA} = 137 \times 10^{-17}$ cm$^2$, which is two orders in magnitude larger than the same figure in SOI waveguides. The free-carrier plasma dispersion coefficient was also found to be many times larger than that of silicon waveguides with a measured value of $k_{FCD} = 13.5 \times 10^{-21}$ cm$^3$ being reported for the porous silicon-based waveguides. The size of the free-carrier effects in pSi are compelling in that only a small volume fraction of the material consists of silicon, indicating that the scale of the carrier-based nonlinearities may possibly be a consequence of excess carriers in the remaining p-doped silicon. Other potential explanations for the enhanced free-carrier effects include modifications to the mode area resulting from higher field concentrations in the remaining silicon and also higher order nonlinearities including electron avalanche multiplication which has been observed in crystalline silicon waveguides at mid-IR wavelengths [25]. In our model, attribution of these potential higher order effects to free-carrier cross-section and dispersion could cause an overestimation of these parameters. Nonetheless, the agreement between the presented macroscopic model and the data indicates a useful means by which to gauge the material platform for prospective applications. These results favor further study of pSi as an alternative silicon material and already suggest that the fast, large carrier-based nonlinearity could be exploited and engineered [26] for specific photonics applications.

The measurements presented in this study were achieved using a new technique that is robust to noise and can be carried out using standard laboratory equipment. In this approach, the pump beam is chopped which creates additional sidebands when nonlinear mixing of the pump and probe beams occurs in the sample. Measuring one of the sidebands along with the heterodyne signal allows common mode phase variations in the probe and reference pulses to be removed as long as the integration time is fast in comparison to the noise fluctuations. Analysis and experimental details were presented that demonstrate how this new approach can be implemented.

## Appendix: two-frequency heterodyning technique

Traditional optical heterodyning detects a difference, or beat, frequency generated by the mixing of two optical waves of different frequency in a square-law photo-detector [27, 28]. This beat frequency has a phase and magnitude that is directly related to the optical phase difference and amplitudes of the constituent fields, thus making optical heterodyning an attractive method for pump-probe spectroscopy.

The fidelity of the heterodyne signal is susceptible to uncontrolled mechanical and thermal effects introduced by sample heating, thermal relaxation of the opto-mechanical components comprising the system, as well as by laser power fluctuations. A comprehensive study of thermal drift in optical heterodyne systems can be found in [29]. These effects introduce instability into the signals of interest and specialized approaches utilizing radio receivers [18, 30, 31] or fast measurements with radio-frequency lock-in detection [19] have been employed to mitigate them. In this study, we introduce a heterodyning technique that detects two heterodyne signals; a technique thus requiring two lock-in detectors or a single lock-in detector with two phase sensitive channels (in this work we used a single Signal Recovery 7270 with dual-phase lock-in detection). A detailed discussion of the two-frequency heterodyning technique is provided in this appendix.

In contrast to conventional pump-probe heterodyne experiments, deleterious thermal drift and power fluctuation effects in the two-frequency technique are managed by additionally chopping our pump signal. Chopping the pump signal produces sidebands at $\pm f_C$ from the heterodyne frequency, where $f_C$ is the chopping frequency. It will be shown that measurement of one of the sidebands in addition to the primary heterodyne signal provides a simple and robust means of eliminating noise, particularly phase drift, in the heterodyne measurement. It

#212659 - $15.00 USD Received 22 May 2014; revised 25 Jun 2014; accepted 26 Jun 2014; published 10 Jul 2014

should also be noted that a judicious choice of the heterodyne frequency to be an odd integer multiple of the chopper half-frequency (i.e., $f_H = N\frac{f_C}{2}$, $N =$ odd integer), spectrally segregates the strong, co-propagating and co-polarized pump signal from the heterodyne signal; further improving the signal to noise ratio of the measurement.

Essential to the success of this method is that a common master clock is used to generate the frequencies driving the AOFSs, the chopper, and the reference input on the lock-in detector. This ensures that a common phase relationship is maintained between all beams and detection hardware in the experiment. For the measurements reported here, we used a four-channel, 171 MHz digital digital signal generator (Novatech Intruments Inc. Model 409B, which incorporates the Analog Devices AD9959 programmable synthesizer chip.) The first two channels were programmed to generate the 35 MHz and 35.0625 MHz signals required to drive the AOFSs. The third channel produces a $f_c = 1$ kHz signal that was used to drive the optical chopper. The fourth output of the synthesizer was programmed to produce a 500 Hz reference frequency equal to half of the chopper frequency that was sent to the lock-in amplifier. The lock-in amplifier was then configured to simultaneously measure at both 62.5 kHz and 63.5 kHz (i.e., the 125th and 127th harmonics of the reference frequency.) The heterodyne frequency is specifically chosen to be an odd integer multiple of the chopper half-frequency, which ensures that there is no interference from higher harmonics of the strong chopped pump pulse.

In order to unambiguously measure the relative phase and intensity shift, the correct phase relationship must be established between the pump beam and the chopper wheel since a phase offset can occur depending on the relative spatial position of the pump beam in the chopper wheel slot and the chopper wheel position with respect to the photo-interrupter in the chopper wheel controller. To eliminate this phase offset, the phase of the detected pump signal at the chopping frequency is zeroed in the lock-in amplifier immediately prior to conducting measurements.

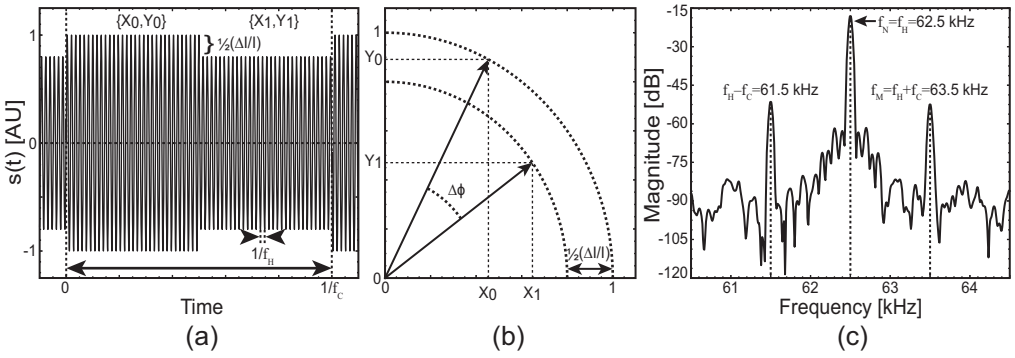


Fig. 5. (a) Notional time series data showing the function $s(t)$ over one chopping period as described by Eq. (6). The chopper wheel blocks or passes the pump beam in time intervals of length $\frac{1}{2f_c}$ with the sinusoidally varying signal in each interval being described by $\{X_0, Y_0\}$ or $\{X_1, Y_1\}$ respectively. (b) Component representation of the notional time series is shown in the first quadrant of the in-phase and quadrature-phase plane. (c) Measured frequency spectrum of $s(t)$ with relevant harmonics indicated. Harmonics of the collinear pump, which occur at even integer multiples of the 0.5 kHz lock-in amplifier reference frequency, are suppressed through the use of balanced detection.

Figure 5 illustrates the principle of operation of the two-frequency lock-in detection, for a fixed pump delay. When the probe and reference pulses interfere with one another in the balanced detector, they produce a sinusoidal heterodyne signal at the heterodyne frequency

#212659 - $15.00 USD Received 22 May 2014; revised 25 Jun 2014; accepted 26 Jun 2014; published 10 Jul 2014

$f_H(= 62.5$ kHz$)$. We note that the detectors used are not fast enough to resolve the individual pulses ($\approx$ 500 fs) or their repetition period (10 ns). As illustrated notionally in Fig. 5(a), the magnitude and phase of the heterodyne signal depends on whether the pump is on or off. When the pump intensity is chopped, the received signal $s(t)$ may be written as a periodic signal:

$$s(t) = \begin{cases} X_1\cos(Nt) + Y_1\sin(Nt) & -\pi < t \leq -\frac{\pi}{2} \\ X_0\cos(Nt) + Y_0\sin(Nt) & -\frac{\pi}{2} < t \leq 0 \\ X_1\cos(Nt) + Y_1\sin(Nt) & 0 < t \leq \frac{\pi}{2} \\ X_0\cos(Nt) + Y_0\sin(Nt) & \frac{\pi}{2} < t \leq \pi \end{cases} \tag{6}$$

In this expression, the the period $2\pi$ represents two full chopping cycles and $N(= 125)$ heterodyne cycles, where $N$ is an odd number. The coefficients $X_0$ and $Y_0$ represent the in-phase and quadrature-phase components of the heterodyne signal when the pump is off, while $X_1$ and $Y_1$ correspond to the in-phase and quadrature-phase components when the pump is on. Figure 5(b) illustrates vector component representation of heterodyne signal when the pump is off and on, illustrating the change in intensity and phase.

Figure 5(c) shows a representative spectrum of the received signal $s(t)$, measured using an electrical spectrum analyzer. In addition to the heterodyne tone at $f_H(= 62.5$ kHz$)$, we see sidebands at $f_H \pm f_C$, where $f_C$ is the chopping frequency (1 kHz.) The lock-in detector is configured to simultaneously measure the Fourier components at $f_H$ and $f_H + f_C$.

The periodic signal $s(t)$ can be expanded in a Fourier series:

$$s(t) = \frac{x_0}{2} + \sum_{n=1}^{\infty} x_n\cos(nt) + y_n\sin(nt) \tag{7}$$

with the expansion coefficients being given by:

$$x_n = \frac{1}{\pi}\int_{-\pi}^{\pi} s(t)\cos(nt)dt, \qquad n = 0,1,2,\ldots \tag{8}$$

$$y_n = \frac{1}{\pi}\int_{-\pi}^{\pi} s(t)\sin(nt)dt, \qquad n = 1,2,\ldots \tag{9}$$

Substituting Eq. (6) into Eqs. (8) and (9), we obtain the following expressions for the Fourier cofficients at the heterodyne frequency ($n = N(= 125)$) and at the first upper sideband ($n = M = N + 2(= 127)$):

$$x_N = \frac{X_0 + X_1}{2} + \frac{Y_1 - Y_0}{\pi N} \tag{10}$$

$$y_N = \frac{Y_0 + Y_1}{2} + \frac{X_1 - X_0}{\pi N} \tag{11}$$

$$x_M = \frac{Y_0 - Y_1}{\pi} \tag{12}$$

$$y_M = \frac{X_1 - X_0}{\pi} \tag{13}$$

The dual-frequency lock-in detector employed in these experiments allows for simultaneous measurement of these four quantities, although we note that with a appropriate reference signals the four quantities could be also measured using two independent lock-in amplifiers. From these four measured quantities, one can calculate the the Fourier coefficients of the heterodyne signal

#212659 - $15.00 USD Received 22 May 2014; revised 25 Jun 2014; accepted 26 Jun 2014; published 10 Jul 2014

when the pump is off ($X_0$, $Y_0$) and on ($X_0$, $Y_0$).

$$X_0 = x_N + \frac{1}{N}x_M - \frac{\pi}{2}y_M \tag{14}$$

$$Y_0 = y_N - \frac{1}{N}y_M + \frac{\pi}{2}x_M \tag{15}$$

$$X_1 = X_0 + \pi y_M \tag{16}$$

$$Y_1 = Y_0 - \pi x_M \tag{17}$$

From these results we can calculate the relative change in intensity, $(\Delta I/I)$, and change in phase, $\Delta\phi$,

$$\left(\frac{\Delta I}{I}\right) = \frac{X_1^2 + Y_1^2}{X_0^2 + Y_0^2} - 1 \tag{18}$$

$$\Delta\phi = \tan^{-1}\left(\frac{Y_1}{X_1}\right) - \tan^{-1}\left(\frac{Y_0}{X_0}\right) \tag{19}$$

This approach subtracts off the intensity and phase noise fluctuations common to both measured harmonics leaving only the change in intensity and phase resulting from the presence of the pump pulse.

For small changes in the relative intensity and phase, or equivalently, when the Fourier amplitudes satisfy $(x_M, y_M) \ll (x_N, y_N)$, Eqs. (18) and (19) can be expanded to first order to give

$$\left(\frac{\Delta I}{I}\right) = 2\pi\left(\frac{x_N y_M - y_N x_M}{x_N^2 + y_N^2}\right) \tag{20}$$

$$\Delta\phi = -\pi\left(\frac{x_N x_M + y_N y_M}{x_N^2 + y_N^2}\right) \tag{21}$$

**Acknowledgments**

We would like to acknowledge the support of the Laboratory for Physical Sciences and the Maryland Nanocenter.

#212659 - $15.00 USD Received 22 May 2014; revised 25 Jun 2014; accepted 26 Jun 2014; published 10 Jul 2014